3-D EM inversion of ground based geomagnetic Sq data. Results from the analysis of Australian array (AWAGS) data

Stephan Koch and Alexey Kuvshinov

Institute of Geophysics, ETH Zürich, Sonneggstrasse 5, 8092 Zürich, Switzerland. E-mail: stephan.a.koch@googlemail.com

SUMMARY

We present the first inversion of geomagnetic Sq data in a framework of 3-D conductivity models. This problem has been considered as immensely difficult due to the complex spatial structure of the Sq source which, in addition, varies with season and solar activity. Recently, we developed a 3-D electromagnetic (EM) inversion solution that allows one to work in a consistent manner with data that originates from sources, irrespective of their spatial complexity. In this paper, we apply our 3-D EM inversion scheme to Sq data collected during the Australian Wide Array of Geomagnetic Stations project. Within this project, three components of the geomagnetic field were recorded between 1989 November and 1990 December with the use of 53 portable vector magnetometers. The instruments were distributed over the Australian mainland with an average spacing of 275 km between sites. Inverting this unique—in a sense of its spatial regularity, density and long operational time—data set, we recovered the 3-D conductivity distribution beneath Australia at upper mantle depths (100–520 km). This depth range was justified in the paper from resolution studies using checkerboard tests. In addition, we performed extensive modelling to estimate quantitatively the influence of various factors on Sq signals, namely from hypothetical anomalies, inaccuracy in the source, ocean, and model discretization. As expected, the ocean (coastal) effect appeared to be the largest so that it has to be accounted for during 3-D inversion as accurately as possible. Our 3-D inversions—of data from either single or multiple days—revealed a strong offshore conductor near the south-east coast of Australia, which persists at all considered depths. Varying in details, this anomaly is remarkably robust irrespective of the considered day(s). We compared our results to those obtained from a different inversion scheme and an independent induction data set, and observed encouraging similarity. Combination of the two results suggests, that this conductor continues to the base of the mantle transition zone at 660 km. The nature of this anomaly is not fully understood but one possible explanation is that it is attributed to a reservoir responsible for three hotspots in the region.

Key words: Numerical solutions; Inverse theory; Geomagnetic induction; Mantle processes.

1 INTRODUCTION

There is great interest to understand the 3-D properties of the Earth's mantle to characterize the dynamics of the deep Earth interior. So far, our knowledge of the 3-D variations of Earth's properties comes mainly from global seismic tomography (Becker & Boschi 2002; Panning & Romanowicz 2006; Kustowski *et al.* 2008, among others). However, the interpretation of the seismic velocity anomalies in terms of thermodynamic and compositional parameters lacks additional and independent information (e.g. Trampert *et al.* 2004; Khan *et al.* 2009). An alternative method to directly recover the physical properties of the mantle is deep electromagnetic (EM) induction sounding, which can potentially probe the 3-D electrical conductivity distribution in the Earth's mantle from time-varying magnetic

field data. To separate the effects of composition and temperature, or to illuminate the role of partial melt and fluids (especially water) in the mantle, both seismic and EM techniques are likely to be important (Khan & Shankland 2012).

However, only recently, through the growth of computational resources and improvements in global 3-D EM forward modelling has the full 3-D EM inversion on a global scale become feasible. In the last decade a few inverse 3-D solutions have been developed (Koyama 2001; Kelbert *et al.* 2008; Tarits & Mandea 2010; Kuvshinov & Semenov 2012), providing the first large-scale (semi-global; Fukao *et al.* 2004; Koyama *et al.* 2006; Utada *et al.* 2009; Shimizu *et al.* 2010; Koyama *et al.* 2014) and global (Kelbert *et al.* 2009; Tarits & Mandea 2010; Semenov & Kuvshinov 2012) 3-D mantle conductivity models. The recent progress in global 3-D

forward and inverse modelling is summarized in the review papers by Kuvshinov (2008, 2012).

All aforementioned studies use disturbed storm-time variations (D_{st}) originating from the magnetospheric ring current, which allow a 3-D recovery of electrical conductivity in the depth range from about 400 down to 1500 km. However, there is great interest in mapping electrical conductivity at upper mantle (UM) depths (100–400 km) since determination of UM conductivity using EM methods can provide constraints on melting processes and the presence of water in the UM. Recent laboratory experiments demonstrate that the electrical conductivity of UM minerals is greatly affected by small amounts of water or by partial melt (Wang *et al.* 2006; Gaillard *et al.* 2008; Yoshino *et al.* 2009, among others). Probing conductivity at UM depths requires EM variations in a period range between a few hours and one day. This is a challenging period range for global EM studies since the ionospheric solar quiet (Sq) source, which dominates this period range, has a much more complex spatial structure than the magnetospheric D_{st} source. The publications of Parkinson (1977), Winch (1981) and Schmucker (1999) discuss the spatial structure of the Sq current system.

Koch & Kuvshinov (2013) presented a novel global 3-D EM inverse solution that allows one to work in a unified and consistent manner with data that originate from ionospheric (and magnetospheric) sources, irrespective of their spatial complexity. This work presents the application of the numerical concept to ground based Sq data collected in the course of the Australian Wide Array of Geomagnetic Stations (AWAGS) project. The data from this unique large, dense and regular network of magnetic field observations allowed us to image the 3-D conductivity distribution beneath Australia down to a depth of 520 km. As far as we know, this is the first attempt to invert experimental Sq data in the frame of 3-D conductivity models.

The paper is organized as follows. In Section 2, we summarize the approach for the Sq source determination and the 3-D inversion scheme. We describe the modifications of the numerical solution scheme to make it applicable to a limited large-scale area instead of a global area as originally presented in Koch & Kuvshinov (2013). In Section 3, we introduce the AWAGS data set and discuss our approach for selecting the quietest days to obtain the data which are used for the inversion. Section 4 presents model studies which aim to quantify the potential resolution of the models obtained from the inversion of AWAGS data, as well as to estimate various effects in Sq signals—from hypothetical deep anomalies, inaccuracy of the source, ocean, and model discretization. The inversion results are presented in Section 5. We first show the results obtained from inversions of single day data in order to demonstrate the robustness of the recovered structures, and subsequently present the final 3-D UM electrical conductivity model beneath Australia obtained from multiple-day inversion. In Section 6, we discuss our inversion results in a context of geodynamic characteristics of the area. A summary of the work presented in the paper and conclusions are given in Section 7.

2 METHOD

2.1 Source determination

To determine the Sq source we exploit the S3D method presented in Koch & Kuvshinov (2013). It is an attractive alternative to the classic potential method of Gauss (1838) as used, for example by Schmucker (1999). The potential method lacks the ability to deal

with a 3-D conductivity model as *a priori* information which is in particular important to account for the ocean effect (Kuvshinov 2008). A detailed explanation of the S3D method is given in Koch & Kuvshinov (2013). The Sq source is represented by specific set of 11 spherical harmonics (SH) coefficients for 24 hr time harmonic and by corresponding sets of 12 SH coefficients for the rest of five time harmonics (12, 8, 6, 4.8 and 4 hr), as suggested by Schmucker (1999).

To determine the source, the data from a global net of observatories and AWAGS data are used. Note that we use the data only from mid-latitude observatories in order to exclude distorting effects from the equatorial and polar electrojets. Here mid-latitude observatories are those located between $\pm 6°$ and $\pm 60°$ geomagnetic latitude. The location of these observatories is shown on the right-hand top plot in Fig. 2. All three components are used for source determination.

2.2 Forward problem solution

The robustness of resolved Earth electrical properties strongly depends on the accuracy of the forward solutions which are used to model the 3-D EM induction. To solve Maxwell's induction equations in a heterogeneous sphere, we use an integral equation (IE) based solver (Kuvshinov 2008). Recent benchmark studies (Kelbert *et al.* 2014) showed, that this solver is fast and accurate, and in many scenarios outperforms the solvers based on alternative approaches (finite difference, finite element and spherical harmonic-finite element). The implementation of the IE solver used in this study exploits the fact that Green's tensors need to be computed only once as long as the background model remains unchanged. This results in a highly efficient application for solving inverse problems where repeated numerical solutions are required. The details of the forward problem and computation of Green's tensors are discussed in Kuvshinov & Semenov (2012).

To allow high resolution modellings of the ocean effect, which is necessary to obtain robust inversion results as discussed later in Section 4, we modified our forward solution in such a way that it is possible to compute the EM field, not on a full sphere, but only in a latitudinal band of the area of interest. The restriction along longitude is not implemented. Since the computational load is scaled to the second order with the used latitudinal nodes and is linear with respect to longitudinal nodes, the efficient calculation mainly benefits from limiting the latitude nodes. In the case of Australia, the latitudinal bounds are in between $+10°$ and $-55°$. On the basis of the model resolution studies (Koch & Kuvshinov 2013) we expect to detect lateral conductivity changes in between 10 and 670 km. We discretize this depth column in 5 layers (10–100, 100–250, 250–410, 410–520 and 520–670 km). The lateral discretization of the forward modelling domain is chosen to be $1° \times 1°$ in agreement with the results of the model studies, discussed in Section 4.

2.3 Inverse problem solution

The inverse problem of conductivity recovery is formulated as minimization of the penalty function

$$\phi(\mathbf{m}, \lambda) = \phi_d(\mathbf{m}) + \lambda \phi_R(\mathbf{m}), \tag{1}$$

where $\mathbf{m} = (\log \sigma_1, \log \sigma_2, \ldots, \log \sigma_N)$ is a vector containing the conductivities in the blocks which comprise the inverse modelling domain, λ is the regularization parameter, $\phi_R(\mathbf{m})$ is the regularization term, $\phi_d(\mathbf{m})$ is the data misfit. The inverse approach is fully

explained in Kuvshinov & Semenov (2012) and Koch & Kuvshinov (2013). For our problem the data misfit $\phi_d(\mathbf{m})$ reads

$$\phi_d(\mathbf{m}) = \sum_{q=1}^{N_d} \sum_{s \in Sites(q)} \sum_{p=1}^{6} \left| Z_s^{m,q}(\mathbf{m}, \omega_p) - Z_s^{e,q}(\omega_p) \right|^2, \quad (2)$$

where $Sites(q)$ defines a set of locations for a given q-th day, and $Z_s^{m,q}(\mathbf{m}, \omega_p)$ and $Z_s^{e,q}(\omega_p)$ are modelled and experimental vertical components of magnetic field, respectively, at location s and angular frequency ω_p. We focus in this study only on the inversion of vertical (Z) component data, since the studies of Koch & Kuvshinov (2013) have demonstrated that the Z component is most sensitive to detect the 3-D electrical conductivity at UM depths from Sq data. The outer sum stresses the fact that we can include data from more than one single day into the inversion as shown in Section 5, where N_d specifies a number of days. Each chosen day is specified by its own source structure, which is known to vary with season and solar activity. In our inverse setup the regularization term $\phi_R(\mathbf{m})$ has the form

$$\phi_R(\mathbf{m}) = (W\mathbf{m})^T (W\mathbf{m}), \quad (3)$$

where T means transpose and matrix W approximates the 3-D spatial gradient. We apply the limited-memory quasi-Newton method to minimize our penalty function in eq. (1). The inversion code was parallelized with respect to period ω_p and number of days N_d.

Note that the inverse modelling domain is chosen to be in between $110°$ to $160°$ longitude and $0°$ to $-45°$ latitude, and has the same (both laterally and vertically) discretization as the forward modelling domain has. The difference in the latitude bounds for the forward and inverse domain is introduced to prevent that potential edge effects from the forward solution manifest in the inversion.

3 DATA

The data we use in this study are Sq variations recorded in the course of the AWAGS project. Within this project, three components of the geomagnetic field (with sampling interval of 1 min) were measured between 1989 November and 1990 December with the use of 53 portable vector magnetometers. The instruments were deployed over the Australian mainland with an average site spacing of 275 km (Chamalaun & Barton 1993). Fig. 1 shows the locations of AWAGS sites and the location of four permanent observatories (CNB, CTA, GNA, and LRM), as well as the availability of the data.

In order to invert Sq data, it is crucial to have a good global description of the source current system. The Sq source determination is based on analysis of the AWAGS data and data from a global net of geomagnetic observatories. Bearing in mind the extreme spatial irregularity of the global net, it is strongly desirable to analyse the data during time spans when the source has a spatial structure that is as simple as possible. The common consensus is, that a spatially simplest Sq source geometry is observed during geomagnetically quiet days. On quiet days, the recorded Sq signal stems from a current system which is driven by atmospheric tides in the ambient magnetic field of the Earth. Campbell (1989), Olsen (1997) and Richmond (1995) provide more details about the physics of Sq. These tides are generated from solar heating of the atmosphere on the sunlit side of the Earth. The Sq current system is flowing at 110 km altitude in the thin ionospheric E-layer and has a double vortex structure with an anticlockwise (clockwise) whorl in the northern (southern) hemisphere and is bounded between $\pm 6°$ and $\pm 60°$ geomagnetic latitude with the whorl centres at around $\pm 35°$ geomagnetic latitude. It is stationary in the Earth–Sun line
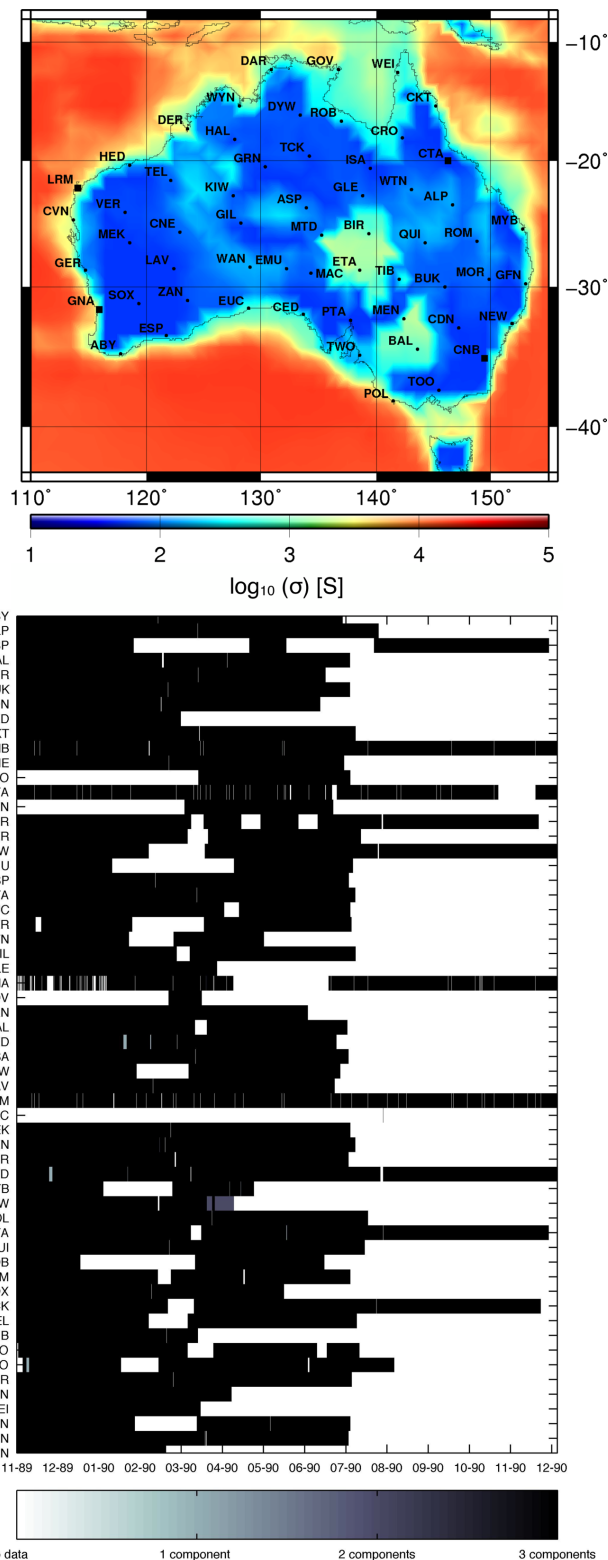

Figure 1. Top panel: positions of the AWAGS sites are plotted on the surface conductance map as developed by Manoj *et al.* (2006). Dots designate the 53 non-permanent vector magnetometers, squares designate the four permanent observatories. Bottom panel: availability of data throughout the operation time of AWAGS. The *y*-axis designates the sites and the *x*-axis—the date, beginning 1989 November and ending 1990 December. The colour coding describes the number of available data components, with black standing for data with all three components (*X*, *Y*, and *Z*) are available and with white standing for no data available.

Table 1. Summary of 49 *truly quiet* Sq days. The concept of *truly quiet* days is discussed in the text. The days are grouped in three subcategories: NS stands for northern summer days, SS for southern summer days and EQ for the equinoctial transition days. INV column represents the status of the inversion results: here S stands for a successful inversion and F for a failed inversion according to the criteria explained in the main text. The column # Obs. contains the total number of observatories on the respective day from the global and *AWAGS* networks, with number of *AWAGS* observatories shown in brackets.

Season	*Sq* day	INV	# Obs.	Season	*Sq* day	INV	# Obs.	Season	*Sq* day	INV	# Obs.
SS	1989-12-09	F	152 (54)	NS	1990-06-30	S	139 (42)	EQ	1990-10-01	F	107 (10)
SS	1989-12-10	S	150 (53)	NS	1990-07-01	F	133 (37)	EQ	1990-10-02	F	106 (9)
SS	1990-01-07	F	147 (52)	NS	1990-07-03	S	138 (38)	EQ	1990-10-17	F	107 (8)
NS	1990-05-06	S	144 (42)	NS	1990-07-07	F	132 (39)	SS	1990-11-03	F	105 (10)
NS	1990-05-07	S	144 (46)	NS	1990-07-16	S	134 (38)	SS	1990-11-04	F	107 (8)
NS	1990-05-15	S	143 (47)	NS	1990-07-17	S	131 (34)	SS	1990-11-05	F	103 (7)
NS	1990-05-16	S	139 (46)	NS	1990-07-22	F	131 (32)	SS	1990-11-06	F	109 (9)
NS	1990-06-02	S	138 (42)	NS	1990-07-23	S	112 (16)	SS	1990-11-12	F	105 (8)
NS	1990-06-03	S	138 (43)	NS	1990-07-24	S	113 (15)	SS	1990-11-13	F	108 (9)
NS	1990-06-04	S	133 (42)	NS	1990-07-25	F	107 (14)	SS	1990-11-14	F	108 (8)
NS	1990-06-16	F	142 (43)	EQ	1990-08-05	S	107 (14)	SS	1990-11-22	F	101 (8)
NS	1990-06-17	S	140 (42)	EQ	1990-08-08	F	106 (8)	SS	1990-11-23	F	107 (8)
NS	1990-06-19	S	137 (40)	EQ	1990-08-09	F	107 (10)	SS	1990-11-24	F	107 (9)
NS	1990-06-20	S	137 (41)	EQ	1990-08-10	F	107 (9)	SS	1990-12-02	F	104 (10)
NS	1990-06-21	S	139 (41)	EQ	1990-09-03	F	106 (9)	SS	1990-12-07	F	101 (7)
NS	1990-06-22	F	139 (42)	EQ	1990-09-30	F	102 (6)	SS	1990-12-10	F	102 (6)
NS	–	–	–	EQ	–		–	SS	1990-12-11	F	99 (3)

due to its solar origin, with the Earth rotating underneath it, and is observed as a local time (LT) phenomenon. Note that the most symmetric structure (with respect to hemisphere balance) of the Sq current system is observed during the quiet days of equinoctial months.

As a threshold to separate quiet days from active days, we use the concept of *truly quiet* days which is based on the geomagnetic *aa*-index (Mayaud 1973). The *aa*-index uses data from two nearly antipodal observatories, which are nowadays the Hartland (HAD) observatory in England and Canberra (CNB) observatory in Australia. With these two stations, which are not influenced by the auroral zone but well balanced in north–south as well as in east–west direction, the geomagnetic *aa*-index is sensitive to the day-night change of the Sq current system. The *aa*-index is provided in nanotesla (nT) and gives an absolute value for the magnetic activity. Following (Mayaud 1973) we characterize the day as *truly quiet* if $aa < 20$ nT over 48 hr, centred on 12:00 LT and 0.00°E. This criterion assures that the actual Sq day of interest is not influenced by an enhanced geomagnetic activity 12 hr before and after the Sq day of interest. Using this criterion as threshold, we found 49 *truly quiet* Sq days during the operation time of AWAGS. The list of these days along with relevant information is presented in Table 1. The time-series of the three components of the magnetic field at each observation site and for the selected days are Fourier transformed, and the corresponding time spectra for six time harmonics are estimated. These spectra serve as input data for the source determination and inversion.

4 MODEL STUDIES

In this section, we first discuss the results of model studies which investigate the horizontal and vertical resolution of the AWAGS Sq data. Further—based, again, on model studies—we estimate quantitatively the effects in predicted Sq variations at the observatory sites of AWAGS from: (i) conductivity anomaly in the UM; (ii) potential inaccuracy in source determination; (iii) ocean–continent contrast; (iv) discretization of the model. For all model studies we use the

same realistic Sq source explained in Table 2. The lateral resolution of the model is $1° \times 1°$, except for the investigation of the effect of model discretization. Also, for all modellings we include the surface shell conductivity model which approximates resistive continents and conductive oceans. The surface shell occupies depths from 0 to 10 km and is specified by the known laterally variable conductance as developed by Manoj *et al.* (2006). Regional and global distributions of the surface conductance are shown on the top map in Fig. 1 and on the right-hand top map in Fig. 2, respectively.

4.1 Resolution studies

We test the resolution of our inverse scheme for the AWAGS site distribution within a multilayer model. The model, along with the surface shell, contains five layers (either laterally homogeneous or inhomogeneous) between 10 and 670 km depth, embedded in the 1-D background section (Fig. 2, right-hand centre plot). Five data sets have been prepared. The first data set is for the 3-D model where the target layer with a laterally inhomogeneous conductivity distribution is located in depth 10–100 km, with other layers being laterally homogeneous and having the conductivity of the 1-D background section. The second data set is for the 3-D model where the target layer with inhomogeneous conductivity is located in depth range 100–250 km, with other layers being laterally homogeneous, and so forth. The conductivity within the inhomogeneous layer has a $11°$ checkerboard structure along longitude and colatitude and varies by $\sigma_b/\sqrt{10}$ and $\sigma_b\sqrt{10}$ from the background conductivity σ_b at the respective depth (*cf.* right-hand bottom map in Fig. 2). With these five data sets we perform a resolution study which is exemplified in Fig. 2 and closely follows that of Kelbert *et al.* (2008) and Koch & Kuvshinov (2013). The *n*th column (from the left- to the right-hand side) corresponds to the 3-D inversion of the *n*th data set, where during the 3-D inversion we assume that all five layers are inhomogeneous and thus we search the conductivity distributions in all these layers. Note that with perfect data the 5×5 matrix of the maps in Fig. 2 should have diagonal form with the true checkerboard conductivity distributions along the diagonal. As expected

Table 2. External SH coefficients obtained for 1990 May 15 day using the S3D method. The coefficients are estimated using data from the global net of observatories and AWAGS data; n and m represent SH degree and order and p designates the time harmonic. These SH coefficients are used for creating synthetic data sets used in Section 4.

		$p = 1$ (24 hr)			$p = 2$ (12 hr)			$p = 3$ (8 hr)			$p = 4$ (6 hr)			$p = 5$ (4.8 hr)			$p = 6$ (4 hr)
n	m	ϵ_n^m [nT]	n	m	ϵ_n^m [nT]	n	m	ϵ_n^m [nT]	n	m	ϵ_n^m [nT]	n	m	ϵ_n^m [nT]	n	m	ϵ_n^m [nT]
–	–	—	1	1	+0.9586+0.9853i	2	2	−0.3426+0.2827i	3	3	−0.1002−0.1338i	4	4	−0.0156+0.2657i	5	5	+0.0068+0.0802i
1	0	+1.9996+3.2794i	2	1	−0.0756−1.0431i	3	2	+0.4086+0.3687i	4	3	−0.1175−0.1059i	5	4	−0.1069+0.0176i	6	5	+0.1715+0.0431i
2	0	−0.2289+1.2141i	3	1	−0.0596−0.4261i	4	2	+0.0122+0.2347i	5	3	−0.1476+0.1978i	6	4	0.0532−0.0895i	7	5	−0.0637−0.0126i
3	0	+0.0046−0.6133i	4	1	+0.3261−0.2887i	5	2	−0.0652+0.1136i	6	3	−0.0081−0.0608i	7	4	0.0819+0.0855i	8	5	+0.0291+0.0134i
1	1	+1.6076+3.8818i	2	2	1.9045−0.2887i	3	3	−01.1285+0.6122i	4	4	−0.3090−0.1591i	5	5	−0.0144−0.1781i	6	6	−0.0952−0.0822i
2	1	+11.0418+3.1566i	3	2	−4.8334−2.3756i	4	3	+1.1827+1.3502i	5	4	−0.1673−0.0368i	6	5	−0.0253−0.0841i	7	6	0.0763−0.0283i
3	1	+3.0276−0.7229i	4	2	−1.2429−0.3065i	5	3	−0.1570−0.2017i	6	4	+0.4448−0.0089i	7	5	−0.0709−0.0230i	8	6	+0.0152−0.0665i
4	1	−3.0972+0.0385i	5	2	+0.5051+0.3269i	6	3	+0.1691−0.3119i	7	4	−0.2748−0.0602i	8	5	0.1119+0.0483i	9	6	−0.0515−0.0241i
2	2	−0.1668+1.0171i	3	3	−0.0909−0.0456i	4	4	−0.2615+0.0099i	5	5	−0.1084−0.3361i	6	6	−0.0947+0.0928i	7	7	−0.0511+0.0434i
3	2	−0.5181−0.3617i	4	3	+0.6386+0.2431i	5	4	−0.5216−0.3806i	6	5	+0.1494+0.1725i	7	6	−0.0096+0.0290i	8	7	−0.1048−0.0765i
4	2	−0.0356−0.7335i	5	3	−0.0180−0.2027i	6	4	−0.0204−0.2360i	7	5	+0.0137+0.2757i	8	6	0.0918−0.0963i	9	7	−0.0040+0.0391i
5	2	+0.5869−0.2334i	6	3	−0.3684+0.0671i	7	4	+0.1888+0.1121i	8	5	−0.0105−0.1090i	9	6	−0.0266−0.0513i	10	7	+0.0029+0.0260i

we find that with AWAGS Sq data we have the best horizontal and vertical resolution at UM depths between 100 and 520 km.

4.2 The anomaly effect

In order to estimate the effect of a heterogeneous conductivity distribution, which we ultimately want to recover from experimental Sq data, we compute magnetic fields with and without a checkerboard anomaly. This anomaly is shown in Fig. 2 and is in the depth range 100–250 km. Top left, top right and bottom left maps in Fig. 3 show the effect in X, Y and Z components, respectively, at positions of AWAGS sites. The effect is defined as a misfit (per site)

$$\phi_{d,s} = \sum_{p=1}^{6} \left| B_{s,a}(\omega_p) - B_{s,b}(\omega_p) \right|^2 . \tag{4}$$

Here $B_{s,a}(\omega_p)$ and $B_{s,b}(\omega_p)$ are the computed magnetic fields for either X, Y or Z component with and without anomaly, respectively, at location s and frequency ω_p. Note that this equation will be used throughout this section and Section 5 to specify quantitatively the amount of the corresponding effect. Bottom right-hand plot in Fig. 3 shows the time-series of the vertical, Z, component at positions of two representative AWAGS sites. We find that an anomaly (of one order of magnitude larger than the background environment) has a slight influence on the phase and a 5 nT maximum influence on the magnitude of the time-series. Regarding the positions of the two observatories on the conducting part of the checkerboard, one might expect a small amplitude and delayed phase due to the induction effect, this is however not observed. Due to the interplay of the surface conductance map and the checkerboard anomaly, the 3-D modelling of the magnetic fields appear to be highly nonlinear. This emphasizes the need of accurate 3-D EM modelings since predictions on the resulting field from 1-D assumptions are no longer valid within a 3-D environment. From visual inspection of the maps we conclude that the effect from the checkerboard anomaly is largest in the Z component thus confirming the finding of Koch & Kuvshinov (2013).

4.3 The source effect

In this section, we estimate the impact of an uncertainty in the source description on the computed magnetic fields. Potential uncertainty mostly arises from the complex spatial structure of the source and irregular data coverage used to determine the source. In order to estimate the effect of an uncertainty in the source description we added Gaussian noise to the SH coefficients (Table 2), which describe the Sq source. Top left, top right, and bottom left maps in Fig. 4 show the source effect in Z component as misfit (eq. 4) between the results computed without and with 5, 10 and 15 per cent noise in the source, respectively. The 3-D model for this model study includes a surface shell and a 1-D conductivity section underneath. We observe a longitudinal dependence of the source effect, best seen for 15 per cent noise, with largest misfits on the western coast and smallest misfits on the eastern coast. Our understanding of this effect is, that Sq is travelling from east to west, crossing ocean–continent–ocean when passing Australia. These large contrasts in conductivity, together with the moving source might cause the observed longitudinal dependence, however further investigation is needed to reveal the nature of this effect. The bottom right-hand plot in Fig. 4 shows the time-series of the Z component at positions of two representative AWAGS sites. From this plot we see that the impact of uncertainty is rather on the amplitude of the field
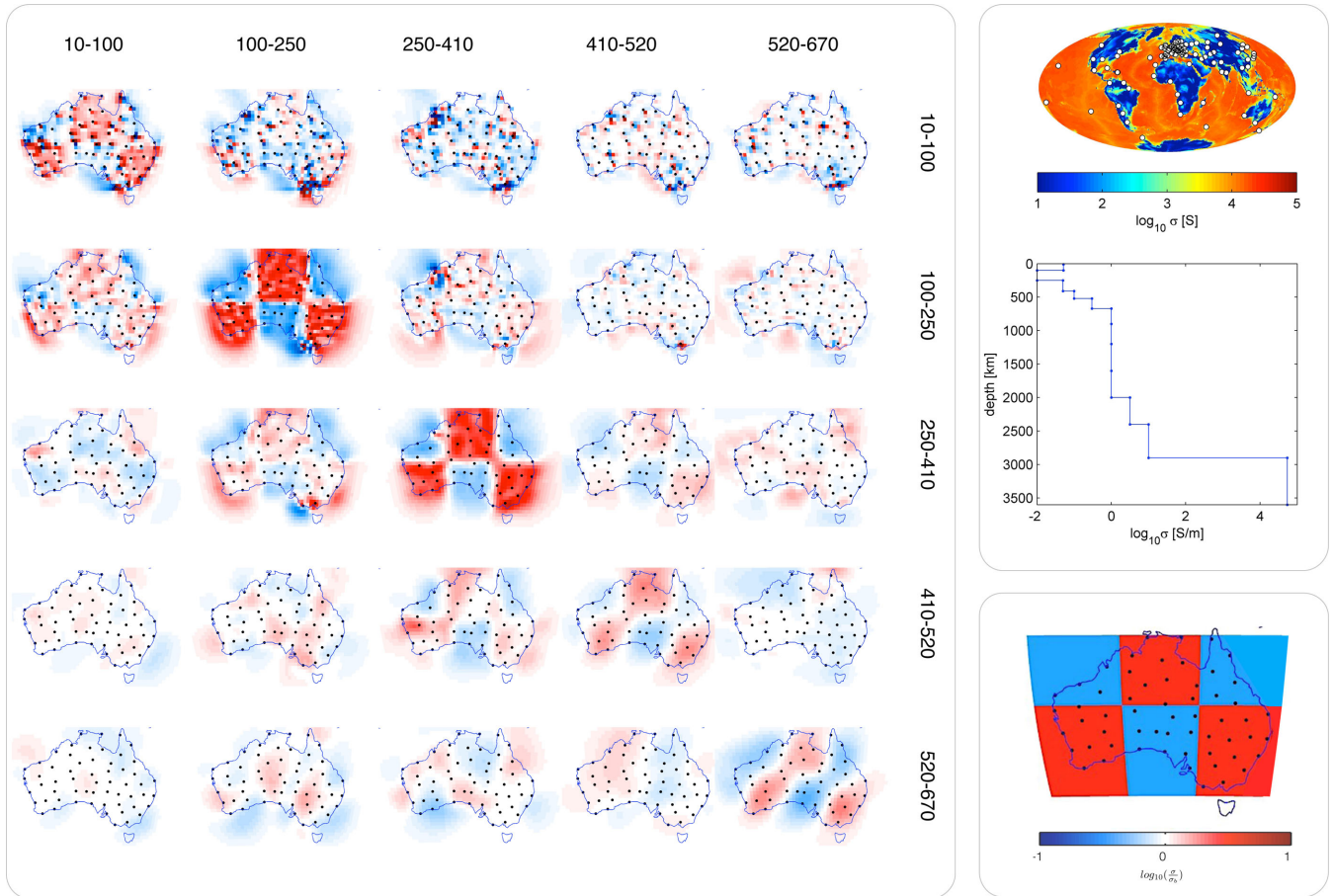
Figure 2. Left-hand panel: results of the resolution study. Every column represents an individual inversion with the target checkerboard anomaly of $\sigma_b/\sqrt{10}$ and $\sigma_b\sqrt{10}$ located at different depths. Numbers on top of each column designate the depth of the checkerboard anomaly, numbers on the right-hand stand for the vertical inverse domain discretization. Conductivities are given in $\log_{10}(\sigma/\sigma_b)$. Right-hand top map: global surface shell conductance map and location (circles) of geomagnetic observatories used for the source determination. Right-hand middle plot: 1-D background conductivity σ_b from Kuvshinov & Olsen (2006). Right-hand bottom map: reference checkerboard of $11°$ anomaly structure embedded into 1-D background section at corresponding depth.

than on the phase. Comparing the source effect with the anomaly effect (*cf*. Fig. 3), we conclude that the effect of the source uncertainty of up to 15 per cent is on average smaller than the anomaly effect.

4.4 The ocean effect

Another effect which needs to be considered when working with geomagnetic time-varying data is the ocean effect. The ocean–continent substantially influences the recorded magnetic fields and needs to be modelled appropriately. This was usually done using a thin spherical shell model of laterally variable conductance, on top of a 1-D radial symmetric shell model as proposed by Price (1949). However Price's model has the following limitation: the shell is galvanically isolated from the 1-D section, which implies that current leakages from the shell into the underlying conductor and vice versa are ruled out. Fainberg *et al.* (1990) presented a bimodal solution which considered galvanic coupling between the shell and underlying 1-D section, thus modelling the ocean effect in the most consistent way. Kuvshinov *et al.* (1999) investigated in detail the ocean effect on geomagnetic fields excited by the Sq and D_{st} source. One of the main findings of their study is, that the

vertical Z component is biased by the oceans practically everywhere on the continents. Only the Eurasian continent appeared to be large enough that the vertical field is undisturbed in the inner mainland. To investigate the problem as quantitatively as possible for our data set, we estimate the ocean effect at the positions of the AWAGS sites.

Top left, top right, and bottom left maps in Fig. 5 show the ocean effect in X, Y and Z components, respectively, as a misfit (eq. 4) between the results computed in the model with and without the surface shell. Note that the shell is underlain by a 1-D conductivity in this model study. As expected, the ocean effect is most prominent in the Z component. Further, it appears to be larger on the east and west coast than on the north and south coast, which can be interpreted as the manifestation of the Sq source travelling along longitude within a fixed mid-latitude corridor. For inland observatories the effect is smaller but still presents. The bottom right-hand plot in Fig. 5 shows the time-series of the Z component at the positions of two representative AWAGS sites. As seen from the plot, the ocean effect heavily influences the phase and the amplitude. Comparing the ocean effect with the anomaly and the source effect (*cf*. Figs 3 and 4) in the most affected Z component, one clearly sees that the ocean effect far exceeds the other effects. This, in particular means, that it should be modelled as accurately as possible. In this
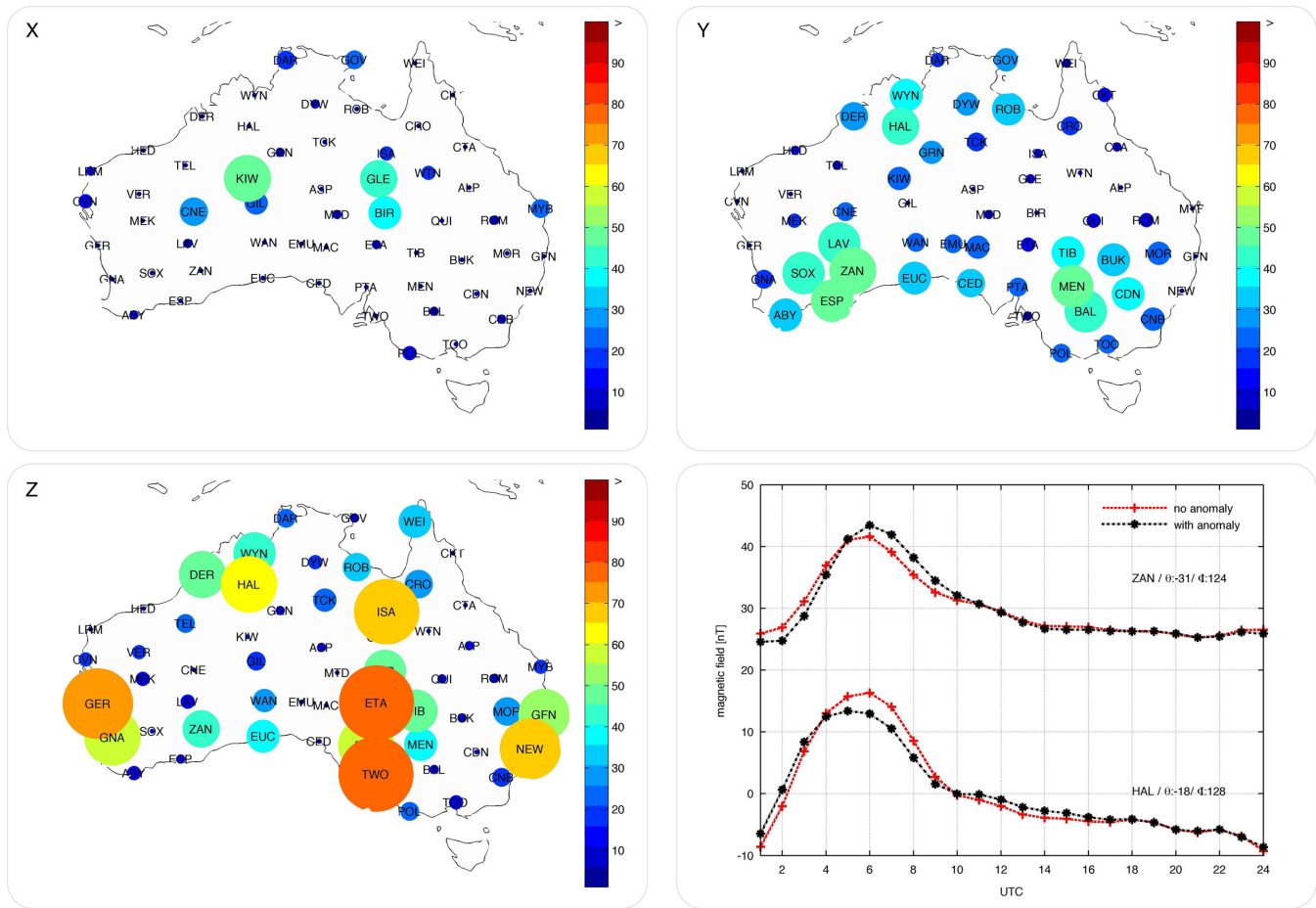
Figure 3. The anomaly effect: top left, top right and bottom left maps show the effect as a misfit (see eq. 4) in *X*, *Y* and *Z*, respectively, between results computed from a 3-D model with and without checkerboard anomaly. The misfits are computed at positions of AWAGS sites. Size and colour reflect the magnitude of the misfit. The checkerboard anomaly is at 100–250 km depth (see conductivity distribution in checkerboard anomaly in Fig. 2, right-hand bottom map). Bottom right-hand plot: time-series of *Z* component of two representative AWAGS sites.

context the question arises, to what detail the ocean effect needs to be modelled. This question is addressed in the next section.

4.5 Effect from model discretization

Top left, top right and bottom left maps in Fig. 6 show the effect in the *Z* component as misfit (eq. 4) between the results computed with $0.25° \times 0.25°$ discretization and with $2° \times 2°$, $1° \times 1°$ and $0.5° \times 0.5°$ discretizations, respectively. The 3-D model for this model study includes the surface shell and 1-D conductivity section underneath. In general, coastal sites are sensitive to ocean/land contrast discretization, with east and west coast sites more influenced. We also conclude from the Fig. 6 that a discretization of $1° \times 1°$ allows for an accurate ocean effect modelling despite of the fact that for a few observatories (LRM, ABY and NEW) the effect from model discretization is comparable for the anomaly effect (see Fig. 3). The bottom right-hand plot in Fig. 6 which shows the time-series of the *Z* component at positions of two representative AWAGS sites which confirm this conclusion. Summarizing all effects, we conclude that a model discretization of $1° \times 1°$ provides a good trade off between computational load and accuracy. It is noted here, that a more accurate modelling of the ocean effect is desired;

however this will only become feasible from future developments of the forward solutions.

5 INVERSION OF AWAGS DATA

In this section, we discuss the results of the 3-D inversion of AWAGS Sq data. We first present the results obtained from inversions of single day data (Section 5.1) in order to demonstrate the robustness of the recovered structures, and subsequently present the final 3-D UM electrical conductivity model based on multiple-day inversion (Section 5.2). During all inversions, the surface shell of known conductance is included in the model, and the 1-D section shown on the right-hand middle plot in Fig. 2 is used as a starting model. Regularization is applied in a such way that the first conductivity distribution is determined with a high regularization parameter λ which leads to a smooth solution with long-wavelength conductivity changes in lateral and vertical direction. As a next step, this solution is used as a starting model for a consecutive inversion run with a smaller regularization parameter λ, and so forth. This backward regularization scheme helps to avoid having the solution trapped in a local minimum and allows a smoother convergence process. To determine the best matching regularization parameter λ in eq. (1) we use the L-curve approach as described in Hansen (1992) where
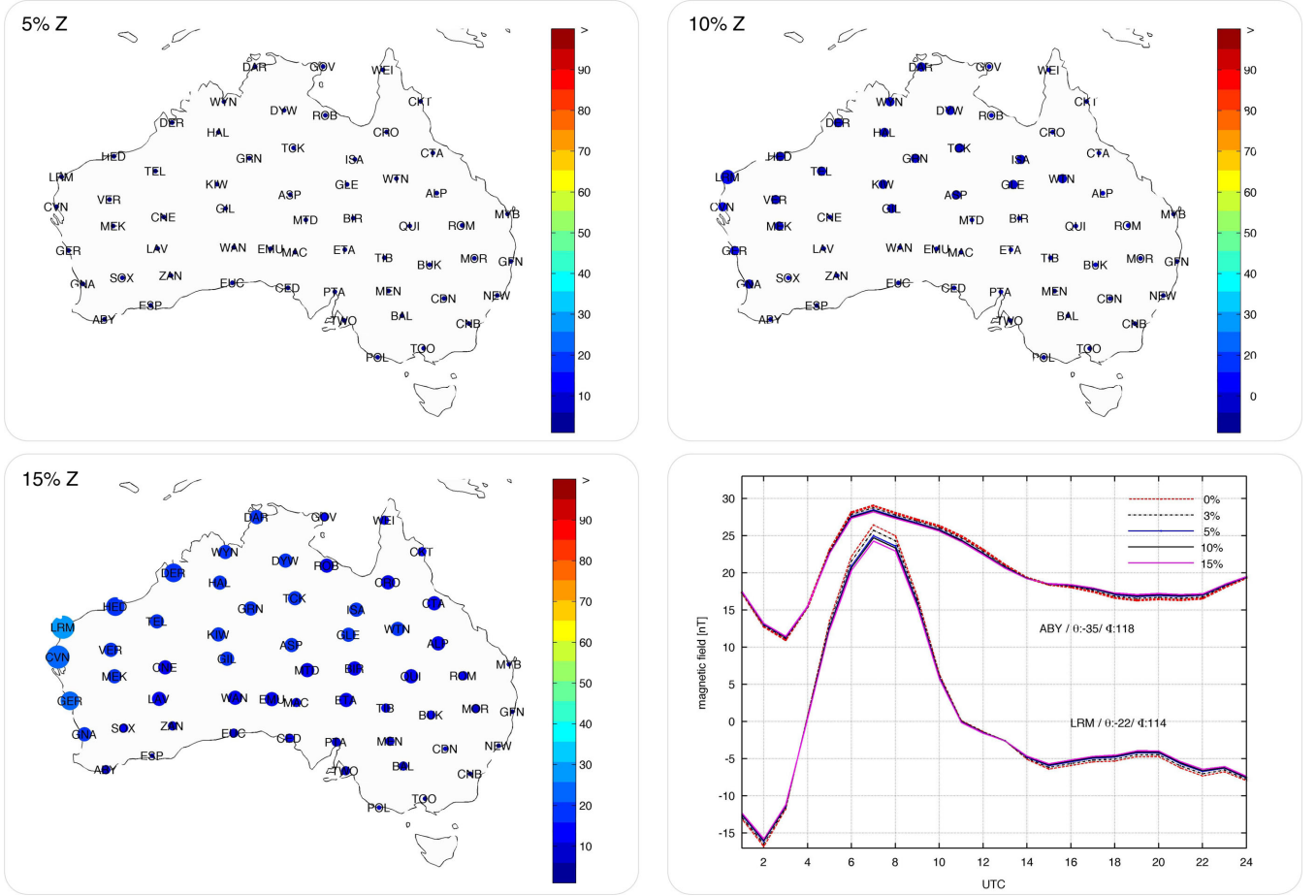
Figure 4. The source effect: top left, top right and bottom left maps show the effect in the *Z* component as misfit (see eq. 4) between the results computed without and with 5, 10 and 15 per cent noise in the source, respectively. The misfits are computed at positions of AWAGS sites. Size and colour reflect the magnitude of the misfit. Bottom right-hand plot: time-series of the *Z* component of two representative AWAGS sites.

it is shown that the optimal regularization parameter lies in the knee of the L-curve.

5.1 Inversion of single days

We invert the *Z* data of the 49 Sq days listed in Table 1. Note that the data analysis starts with the source determination for each specific day. We consider an inversion run to be 'successful' if: (1) the day has a reasonable spatial coverage with AWAGS data ($N_{Sites} \geq 10$); (2) the solution converges after a number of iterations as exemplified in Fig. 7; (3) the total misfit is reduced (see eq. 2); (4) the misfit per site is reduced or at least remains unchanged. In total 19 out of 49 Sq days are successfully inverted (see Table 1) according to these criteria. Note that for the most 'failed' days criterium (1) was decisive. Since the distribution of AWAGS observatories at the end of the survey is rather a profile from north to south than an array, it is unlikely that this allows for a robust 3-D inversion.

Inversion results for six representative days are presented in the second, third and fourth rows (from the top) in Fig. 9. Since our resolution study has shown that the Sq data lacks of sensitivity in the depth range 10–100 km and below 520 km, the conductivity images are presented in then depth range 100–520 km. The results are shown on a logarithmic scale and as a deviation from the background value σ_b. To give an idea of the day-to-day variability of the Sq source,

the first row in Fig. 9 shows the snapshot of the Sq source system over Australia at 04:00 of universal time (UT) as a current function attributed to the surface of the Earth ($a = 6371$ km)

$$\Psi(\vec{r}, t) = Re\left(\frac{a}{\mu_0} \sum_{p=1}^{6} \sum_{n,m} \frac{2n+1}{n+1} \epsilon_n^m(\omega_p) Y_n^m(\theta, \phi) e^{iw_p t} \right). \qquad (5)$$

Here $Y_n^m(\theta, \phi)$ are spherical harmonics (SH), μ_0 is magnetic permeability of free space, $\vec{r} = (a, \theta, \phi)$, and $\sum_{n,m}$ is a short expression for the double sum over SH degree *n* and order *m*. The fifth and sixth rows in the figure demonstrate misfits (per site) between observations and predictions from initial, and final (recovered) models, respectively. In addition, Fig. 8 presents time-series of observed *Z*, and *Z* predicted from starting and recovered 3-D models for six representative AWAGS sites for the Sq day 1990-06-02. For completeness Fig. 7 shows the evolution of the (total) misfit and respective L-curve for the same day data.

Analysing the inversion results presented in Fig. 9, we see that they all show a strong positive (conductive) offshore anomaly near the south-east coast of Australia. Varying in details, this feature appears to be remarkably robust irrespective of the considered day (and thus source structure). One can argue that this anomaly could be a manifestation of the ocean (coast) effect which is probably not fully accounted for with the existing conductance map and the adopted resolution. To investigate if the used conductance map,
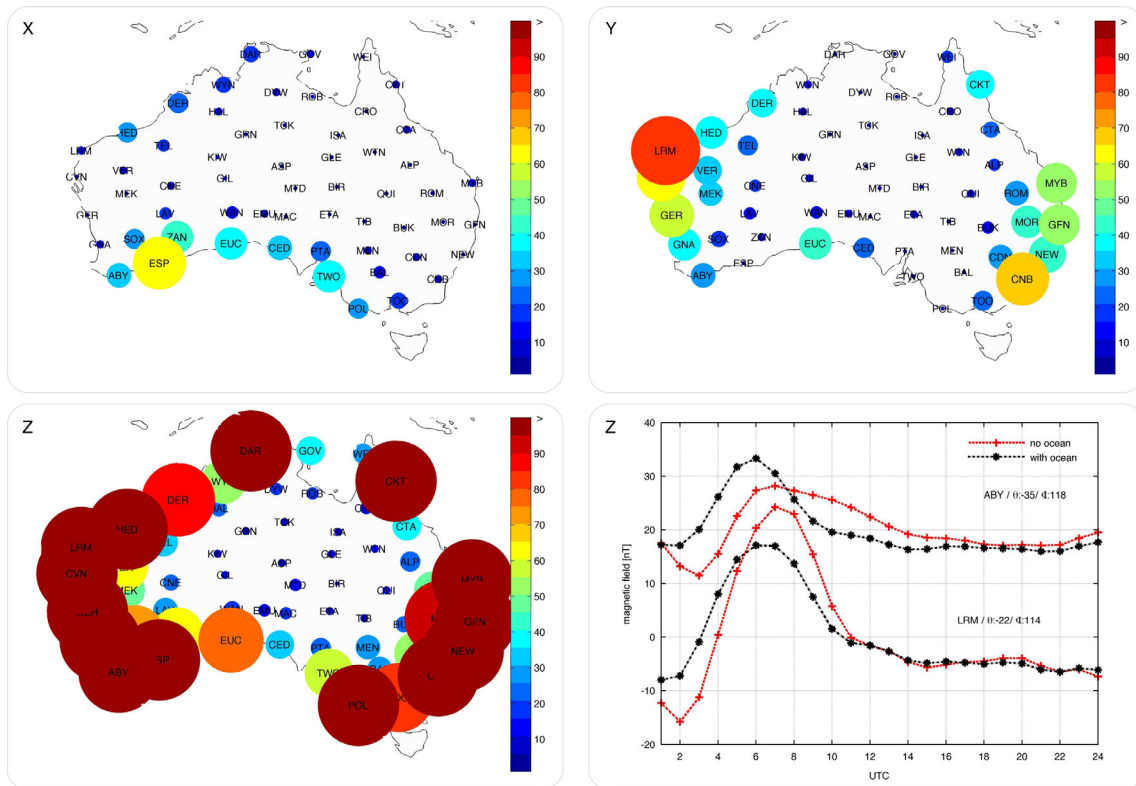
Figure 5. The ocean effect: top left, top right and bottom left maps show the effect as misfit (see eq. 4) in *X*, *Y* and *Z*, respectively, between results computed from a model with and without the surface shell. The misfits are computed at positions of the AWAGS sites. Size and colour reflect the magnitude of the misfit. Bottom right-hand plot: time-series of the *Z* component of two representative AWAGS sites.
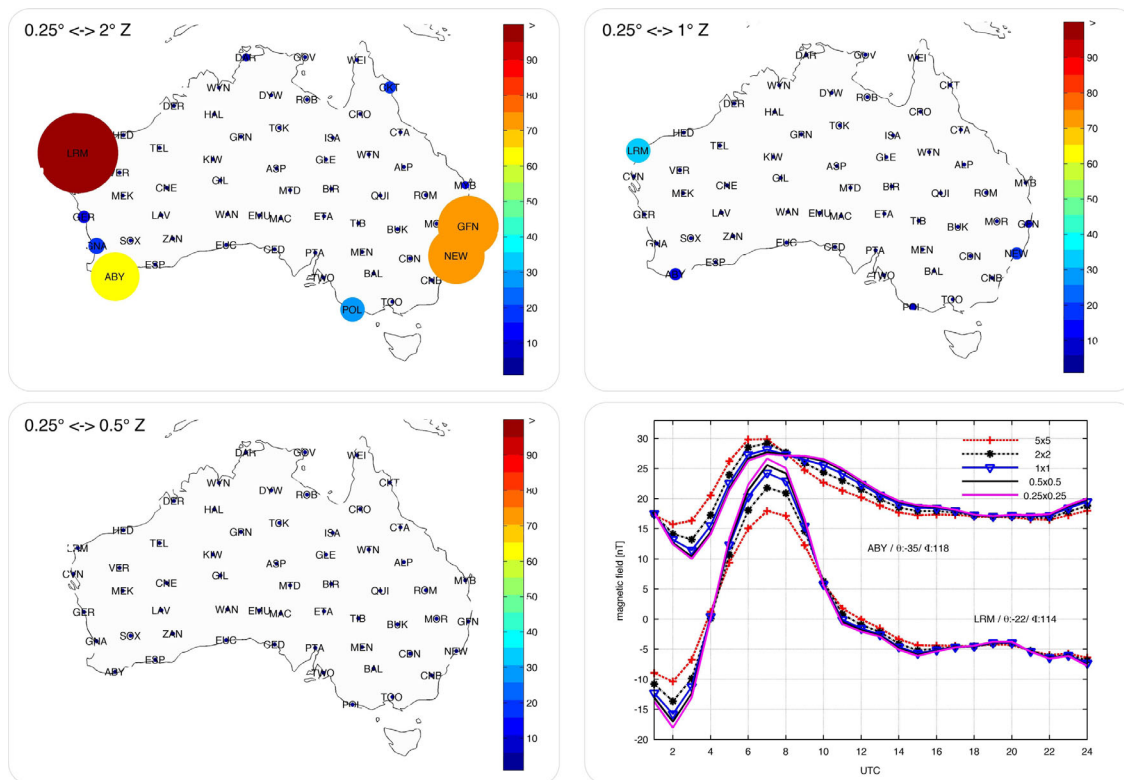

Figure 6. Effect from model discretization: top left, top right and bottom left maps show the effect in the *Z* component as misfit (see eq. 4) between the results computed with 0.25° × 0.25° discretization and with 2° × 2°, 1° × 1° and 0.5° × 0.5° discretization, respectively. The misfits are computed at positions of the AWAGS sites. Size and color reflect the magnitude of the misfit. Bottom right-hand plot: time-series of *Z* component of two representative AWAGS sites.
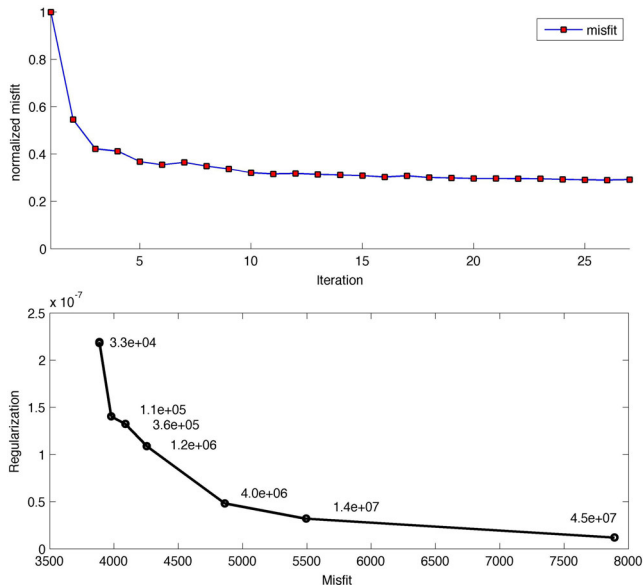
Figure 7. Top panel: evolution of (normalized) misfit during inversion of the data from Sq day 1990-06-02. Bottom panel: L-curve for the same data.
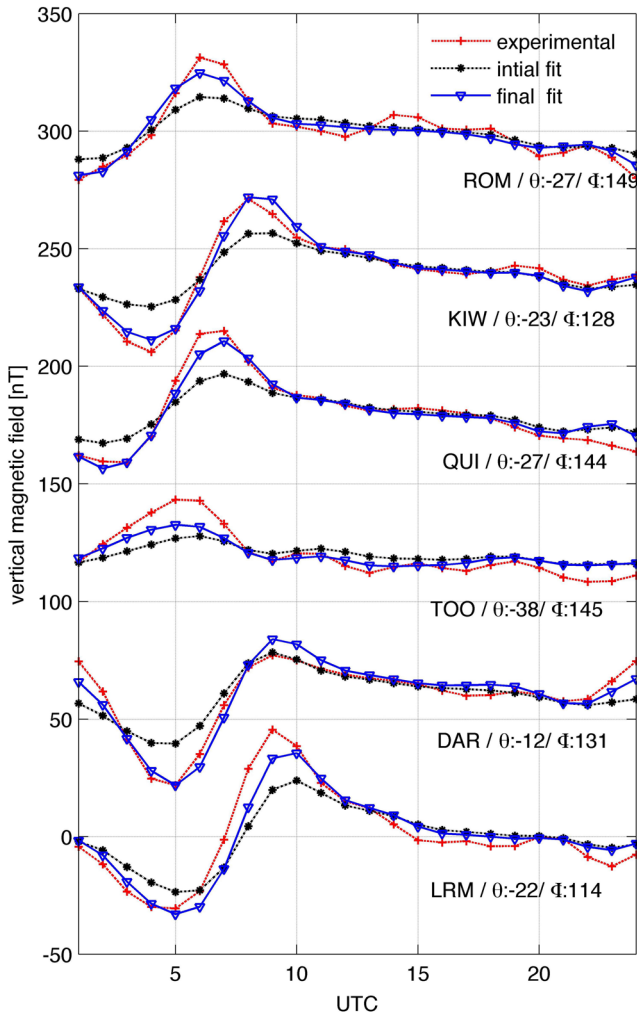

Figure 8. Time-series of *Z* for representative AWAGS sites for the Sq day 1990-06-02. Red line shows the experimental time-series, black and blue lines the time-series predicted from starting and final 3-D models, respectively.

which is based on bathymetry, sediment thickness, salinity, pressure and temperature, affects the inversion results, we executed the inversion with an alternative conductance map, based only on bathymetry and sediment thickness. We found only marginal influence on the inversion results which affected mostly the amplitude of the recovered conductivity, the main features however remained unchanged. Further, there are at least two reasons, not to attribute this anomaly to the ocean effect. First, as seen from Fig. 5, the ocean effect is equally large on the west and the east coasts of Australia. This means that if the ocean effect were responsible for the anomalies in the images they should be seen offshore on both coasts, which is obviously not the case. Second, the number of sites varies from day to day, with overall tendency to decrease with increasing operation time of the AWAGS project. However the anomaly is clearly detected even for the days when the data from many coastal observatories on the east are not available, meaning that also inland observatories pick up the anomaly.

Discussing the inversion results with respect to the misfit per site (see the results in fifth and sixth rows in Fig. 9), we find a good improvement in the area of the anomaly for inland observatories and west coast observatories. However, we observe that a few observatories (mostly on the north coast) show a large initial misfit which is not noticeably improved during inversion. The reason for this is not clear, and we plan to investigate this problem in a separate study.

5.2 Inversion of multiple days

The results of the multiple day inversion are shown in Fig. 10 (labelled as 'Model Sq'), for which 19 successful days were processed (see Table 1 for details). Note again that the source geometry and the available AWAGS sites vary from day to day. We consider the 3-D model obtained during this inversion as the final model of the study. As before, we present the results in the depth range 100–520 km. Remarkably, we are able to reproduce the main features discovered by single day inversions, which comprise an offshore conductive anomaly southeast of Australia and the resistive mainland. Overall, the recovered conductivity distribution appears to be smoother, but the strength of the conductive anomaly is comparable with that obtained from single day inversions (*cf.* Fig. 9).

6 DISCUSSION AND INTERPRETATION

Recently, Koyama *et al.* (2014) presented a 3-D electrical conductivity model beneath Australia at mid mantle depths. They inverted *C*-responses estimated by Semenov & Kuvshinov (2012) from very long time-series of hourly means (1957–2007) recorded at a regional network of eight Australian geomagnetic observatories. The responses were estimated in the period range 4–100 d, on the assumption that the source of the corresponding variations is a symmetric large-scale magnetospheric ring current described by the first zonal harmonic in geomagnetic coordinates. The target depth range was 410–1600 km, discretized by five layers of thickness 410–520, 520–660, 660–900, 900–1200 and 1200–1600 km. Laterally the conductivities were sought in blocks of 5° × 5° size. The maps labelled as 'Model C' in Fig. 10 present their results in the depth range 520–900 km. One can see a positive (conductive) anomaly in the depth range 520–900 km—most prominent at 520–660 km depth—in the south-east part of Australia. This is in remarkable agreement with our results (*cf.* maps labelled 'Model Sq' in the same figure) which also show an enhanced conductivity
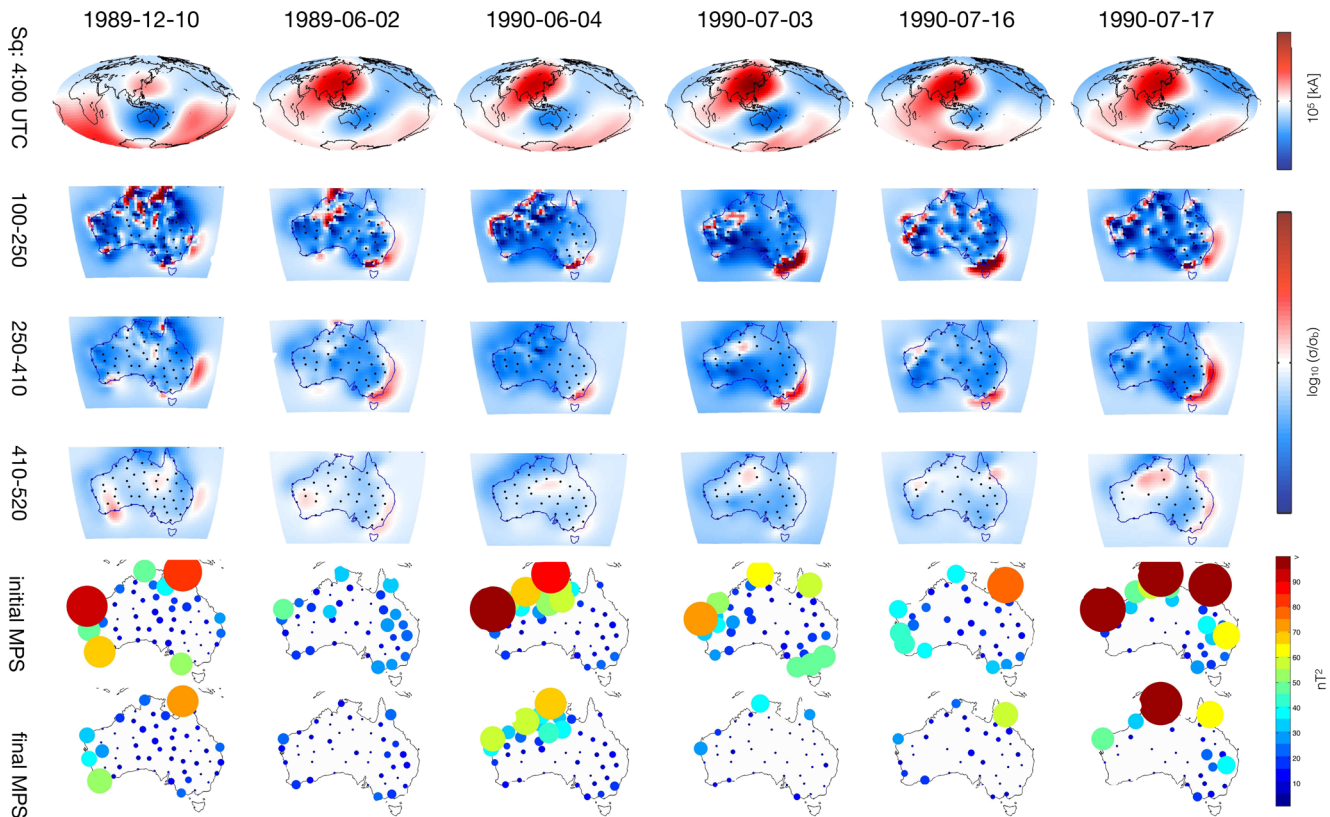
Figure 9. Results of single-day inversions: each of the six columns represents the results for one individual Sq day. Top line specifies the day and is followed by snapshot of Sq source (in a form of current function; see eq. 5) at 4:00 of UT. Second, third and fourth rows present inversion results in three layers. The depth of these layers in [km] is shown on the far left-hand side. Two bottom rows demonstrate the misfits (per site) between observations and predictions from starting (initial), and final (recovered) models, respectively. Colour and size reflect the magnitude of the misfit.

in the same region but at shallower depths. Despite the fact that the resolution is not directly comparable we can conclude from the results of Koyama *et al.* (2014) and this study that there exists a conductive anomaly in the region which is traced from 100 km down to 660 km.

The position of this anomaly correlates well with the position of three hotspots and the seamount chains in the region. On the east coast of Australia, in the Tasman Basin, a chain of generally flat-topped, submarine mountains is detected, the so-called Tasmantid Seamount and the Lord Howe Seamount chains (see Fig. 10 for the position of the chains). The Seamounts were built upon oceanic crust that was generated by seafloor spreading processes in the Late Cretaceous/Early Cenozoic. McDougall & Duncan (1988) investigated if the Tasmantid Seamount chain of volcanoes is a hotspot trail which is recording the movements of the Australian lithospheric plate. Dating of basalt samples of the Tasmantid Seamount chain yield ranges of 24 to 6.4 Ma with progressive rejuvenation of the volcanism southward with an average rate of 67 ± 5 mm yr^{-1}. Further, in accordance with the study of Steinberger (2000) three hotspots are detected in this area (see Fig. 10), namely the Lord Howe, Tasmanid and the East Australian hotspots. A topic of debate concerning the hotspot mechanism is, whether the hotspot reservoir depth is on the top of the D'' layer (2900 km) or at the seismic 660 km discontinuity (Steinberger 2000). Our results give strong evidence that the hotspots arise from a reservoir that occupies even shallower depths.

7 SUMMARY OF RESULTS AND CONCLUSIONS

To the best of our knowledge, this is the first ever attempt to invert geomagnetic Sq data in a frame of 3-D conductivity models. For many years this problem has been considered as extremely challenging due to the complex spatial structure of the Sq source which, in addition, varies with season and solar activity. Recently, we developed a 3-D EM inverse solution that allows one to work in a unified and consistent manner with the data that originate from the sources irrespective of their spatial complexity (Koch & Kuvshinov 2013). By applying this formalism to unique AWAGS data (in the sense of its spatial regularity, density and long operation time), we recovered a 3-D conductivity distribution beneath Australia at UM depths (100–520 km). This depth range was justified in the paper by model resolution studies using multilayer checkerboard tests.

In addition we performed extensive modellings to estimate the magnitude of various effects in predicted Sq signals—from hypothetical anomalies, inaccuracy in the source, ocean and model discretization. As expected, the ocean (coastal) effect appeared to be the largest amongst others having maximum manifestation on the west and east coasts of Australia. This, in particular, means that the ocean effect should be accounted for during inverse modelling as accurate as possible.

Our 3-D inversions of AWAGS Sq data—either single or multiple days—revealed a strong offshore conductor near the southeast coast of Australia, which persists at all considered depths. Varying
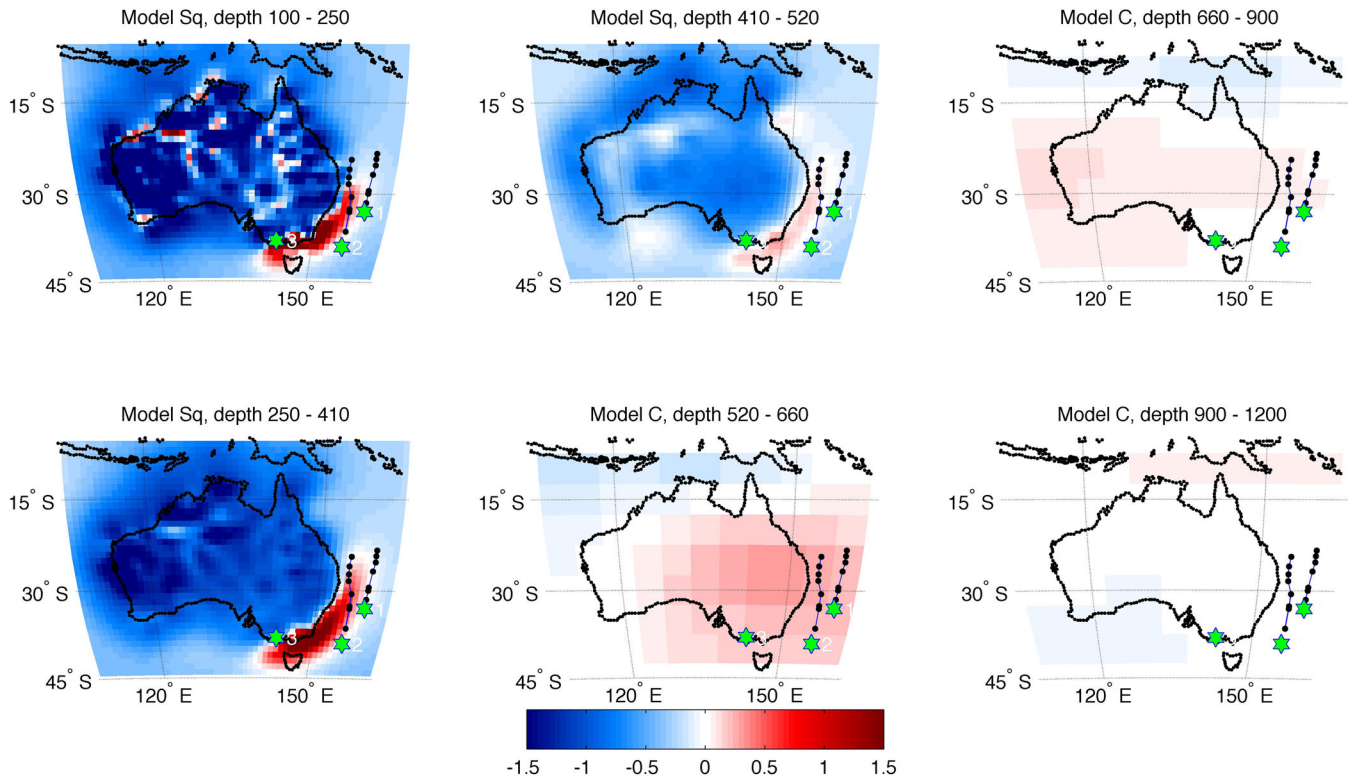
Figure 10. Results of the multiple day inversion (labelled as 'Model Sq'). Also shown are results from the independent induction study of Koyama *et al.* (2014), labelled as 'Model C'. Note that their results are for depth range of 520–1200 km, whereas our results are for depth range of 100–520 km. Green asterisks at each plot show the location of three hotspots—(1) Lord Howe, (2) Tasmanid and (3) East Australia—according to Steinberger (2000). Black small circles show the positions of Tasmantid and Lord Howe Seamount chains (McDougall & Duncan 1988), which are linear chains of submarine volcanoes in the Tasman Basin with progressive rejuvenation of the volcanism southward from 24 Ma (north) to 6.4 Ma (south).

in details, this anomaly is remarkably robust irrespective of days considered. We compared our results with those obtained from a different inverse scheme and independent data set (Koyama *et al.* 2014). They found a 3-D conductivity structure in the deeper mantle (520–660 km) which is similar in position and strength. Combination of the two models suggests a strong conductor, continuing from 100 to 660 km. The nature of this conductor is not fully understood but could be attributed to a reservoir responsible for hotspots and submarine seamounts in the region.

ACKNOWLEDGEMENTS

REFERENCES

Becker, T.W. & Boschi, L., 2002. A comparison of tomographic and geodynamic mantle models, *Geochem. Geophys. Geosyst.,* **3,** doi:10.129/2001GC000168.

Campbell, W., 1989. *The Regular Geomagnetic Field Variations during Solar Quiet Conditions,* Vol. 3, Geomagnetism, Elsevier.

Chamalaun, F. & Barton, C., 1993. Electromagnetic induction in the Australian crust: results from the Australia-Wide Array of Geomagnetic Stations, *Explor. Geophys.,* **24,** 179–186.

Fainberg, E., Kuvshinov, A. & Singer, B., 1990. Electromagnetic induction in a spherical Earth with non-uniform oceans and continents in electric contact with the underlying medium, I. Theory, method and example, *Geophys. J. Int.,* **102,** 273–281.

Fukao, Y., Koyama, T. & Obayashi, M., 2004. Trans-Pacific temperature field in the mantle transition region derived from seismic and electromagnetic tomography, *Earth planet Sci. Lett.,* **217,** 425–434.

Gaillard, F., Malki, M., Iacono-Marziano, G., Pichavant, M. & Scaillet, B., 2008. Carbonatite melts and electrical conductivity in the asthenosphere, *Science,* **322,** 1363–1365.

Gauss, C.F., 1838. *Allgemeine Theorie des Erdmagnetismus. Resultate aus der Beobachtung des magnetischen Vereins im Jahre 1838,* translated by Sabine, E. & Taylor, R., Vol. 2, Scientific Memoirs Selected from the Transactions of Foreign Academies and Learned Societies and from Foreign Journals.

Hansen, P., 1992. Analysis of discrete ill-posed problems by means of the L-curve, *SIAM Rev.,* **34,** 561–580.

Kelbert, A., Egbert, G.D. & Schultz, A., 2008. Non-linear conjugate gradient inversion for global EM induction: resolution studies, *Geophys. J. Int.,* **173,** 365–381.

Kelbert, A., Schultz, A. & Egbert, G., 2009. Global electromagnetic induction constraints on transition-zone water content variations, *Nature,* **460,** 1003–1006.

Kelbert, A., Kuvshinov, A., Velimsky, J., Koyama, T., Ribaudo, J., Sun, J., Martinec, Z. & Weiss, C.J., 2014. Global 3-D electromagnetic forward modelling: a benchmark study, *Geophys. J. Int.,* **197,** 785–814.

Khan, A. & Shankland, T.J., 2012. A geophysical perspective on mantle water content and melting: inverting electromagnetic sounding data using laboratory-based electrical conductivity profiles, *Earth planet. Sci. Lett.,* **27-43,** 317–318.

Khan, A., Boschi, L. & Connolly, J.A.D., 2009. On mantle chemical and thermal heterogeneities and anisotropy as mapped by inversion of global surface wave data, *J. geophys. Res.,* **114,** B09305, doi:10.1029/2009JB006399.

Koch, S. & Kuvshinov, A., 2013. Global 3-D EM inversion of Sq variations based on simultaneous source and conductivity determination: concept validation and resolution studies, *Geophys. J. Int.,* **195,** 98–116.

Koyama, T., 2001. A study on the electrical conductivity of the mantle by voltage measurements of submarine cables, *PhD thesis,* University of Tokyo.

Koyama, T., Shimizu, H. & Utada, H., 2006. Water content in the mantle transition zone beneath the North Pacific derived from the electrical conductivity anomaly, *Am. geophys. Un. Monogr. Ser.,* **168,** 171–179.

Koyama, T., Khan, A. & Kuvshinov, A., 2014. Three-dimensional electrical conductivity structure beneath Australia from inversion of geomagnetic observatory data: evidence for lateral variations in transition-zone temperature, water content and melt, *Geophys. J. Int.,* **196**(3), 1330–1350.

Kustowski, B., Ekstrom, G. & Dziewonski, A.M., 2008. Anisotropic shear-wave velocity structure of the Earth's mantle: a global model, *J. geophys. Res.,* **113**(B6), doi:10.1029/2007JB005169.

Kuvshinov, A., 2008. 3-D global induction in the oceans and solid Earth: recent progress in modeling magnetic and electric fields from sources of magnetospheric, ionospheric and oceanic origin, *Surv. Geophys.,* **29**(2), 139–186.

Kuvshinov, A. & Olsen, N., 2006. A global model of mantle conductivity derived from 5 years of CHAMP, Ørsted, and SAC-C magnetic data, *Geophys. Res. Lett.,* **33,** L18301.

Kuvshinov, A., Avdeev, D.B. & Pankratov, O.V., 1999. Global induction by Sq and Dst sources in the presence of oceans: bimodal solutions for non-uniform spherical surface shells above radially symmetric earth models in comparison to observations, *Geophys. J. Int.,* **137**(3), 630–650.

Kuvshinov, A.V., 2012. Deep electromagnetic studies from land, sea, and space: progress status in the past 10 years, *Surv. Geophys.,* **33,** 169–209.

Kuvshinov, A.V. & Semenov, A.A., 2012. Global 3-D imaging of mantle electrical conductivity based on inversion of observatory C-responses — I. An approach and its verification, *Geophys. J. Int.,* **189,** 1335–1352.

Manoj, C., Kuvshinov, A., Maus, S. & Lühr, H., 2006. Ocean circulation generated magnetic signals, *Earth, Planets Space,* **58,** 429–439.

Mayaud, P., 1973. A Hundred Years Series of Geomagnetic Data 1868–1978, *IAGA Bull.,* **33,** 255 pp.

McDougall, I. & Duncan, R.A., 1988. Age progressive volcanism in the Tasmantid Seamounts, *Earth planet. Sci. Lett.,* **89**(2), 207–220.

Olsen, N., 1997. *Geomagnetic Tides and Related Phenomena*, chapter of *Tidal Phenomena,* Springer.

Panning, M. & Romanowicz, B., 2006. A three dimensional radially anisotropic model of shear velocity in the whole mantle, *Geophys. J. Int.,* **167**(1), 361–379.

Parkinson, W.D., 1977. An analysis of the geomagnetic diurnal variations during the International Geophysical year, *Bull. 173,* Australian Government Publ. Service, Canberra.

Price, A.T., 1949. The induction of electric currents in non-uniform thin sheets and shells, *Quart. J. Mech. Appl. Math.,* **2**(3), 283–310.

Richmond, A.D., 1995. Ionospheric electrodynamics, in *Handbook of Atmospheric Electrodynamics,* pp. 249–290, ed. Volland, H., CRC Press.

Schmucker, U., 1999. A spherical harmonic analysis of solar daily variations in the years 1964–1965: response estimates and source fields for global induction — I. Methods, *Geophys. J. Int.,* **136,** 439–454.

Semenov, A.A. & Kuvshinov, A.V., 2012. Global 3-D imaging of mantle electrical conductivity based on inversion of observatory C-responses — II. Data analysis and results., *Geophys. J. Int.,* **191,** 965–992.

Shimizu, H., Utada, H., Baba, K., Koyama, T., Obayashi, M. & Fukao, Y., 2010. Three-dimensional imaging of electrical conductivity in the mantle transition zone beneath the North Pacific Ocean by a semi-global induction study, *Phys. Earth planet. Inter.,* **183,** 262–269.

Steinberger, B., 2000. Plumes in a convecting mantle: models and observations for individual hotspots, *J. geophys. Res.,* **105**(B5), 11 127–11 152.

Tarits, P. & Mandea, M., 2010. The heterogeneous electrical conductivity structure of the lower mantle, *Phys. Earth planet. Inter.,* **183,** 115–125.

Trampert, J., Deschamps, J., Resovsky, J. & Yuen, D., 2004. Chemical heterogeneities throughout the lower mantle, *Science,* **306,** 853–855.

Utada, H., Koyama, T., Obayashi, M. & Fukao, Y., 2009. A joint interpretation of electromagnetic and seismic tomography models suggests the mantle transition zone below Europe is dry, *Earth planet. Sci. Lett.,* **281,** 249–257.

Wang, D., Mookherjee, M., Xu, Y. & Karato, K., 2006. The effect of water on the electrical conductivity of olivine, *Nature,* **443,** 977–980.

Winch, D.E., 1981. Spherical harmonic analysis of geomagnetic tides 1964–65, *Phil. Trans. R. Soc. Lond., A.,* **303,** 1–104.

Yoshino, T., Matsuzaki, T., Shatskiy, A. & Katsura, T., 2009. The effect of water on the electrical conductivity of olivine aggregates and its implications for the electrical structure of the upper mantle, *Earth planet. Sci. Lett.,* **288,** 291–300.